Study on Quasi-Periodic Oscillations of Black Hole X-Ray Binary Swift J1727.8–1613 with the Insight-Hxmt Observations During 2023 Outburst

Yi Wen , Ai-Jun Dong * , Chao Huang

Posted Date: 8 April 2025

doi: 10.20944/preprints202504.0693.v1

Keywords: Accretion disk; Black hole physics - X-ray binary: Individual (Swift J1727.8-1613)

 doi:10.20944/preprints202504.0693.v1

Article

Study on Quasi-Periodic Oscillations of Black Hole X-Ray Binary Swift J1727.8-1613 with the Insight-HXMT Observations During 2023 Outburst

Yi Wen [1,2], Ai-Jun Dong [1,2,*] and Chao Huang [1,2]

[1] School of Physics and Electronic Science, Guizhou Normal University, Guiyang 550001, China
[2] Guizhou Provincial Key Laboratory of Radio Data Processing, Guiyang, China
* Correspondence: aijdong@gznu.edu.cn

Abstract: The X-ray timing properties serve as crucial tool to understand the physical mechanism, such as accretion and jet physics, of black hole X-ray binary (BH XRBs). The study carried out a systematic timing analysis of the Swift J1727.8-1613. The observational data come from the Hard X-ray Modulation Telescope (Insight-HXMT) in 2023, when Swift J1727.8-1613 was transitioning from low-hard state (LHS) to the hard-intermediate state (HIMS). We analyzed their power density spectrum (PDS) and find an obvious type-C quasi-periodic oscillations (QPOs) with the QPO frequency increasing from 0.2 Hz to 1.8 Hz. Detailed light curve and power spectral analysis revealed that the root-mean-square (RMS) amplitude of the QPOs gradually decreased from ∼14% to ∼10%. These observational characteristics show excellent agreement with predictions from the Lense-Thirring precession model under the truncated disk scenario, suggesting that the increasing precession frequency results from the inward migration of the inner accretion disk radius.

Keywords: accretion disk; black hole physics - X-ray binary: Individual (Swift J1727.8-1613)

1. Introduction

Based on the mass of the companion star, black hole X-ray binary (BH XRBs) can be classified into high-mass X-ray binaries (HMXBs) and low-mass X-ray binaries(LMXBs). BH XRBs spend most of their time in a quiescent state, where the accretion rate is low and the X-ray radiation is too weak to be detected. As accretion proceeds, material from the companion star overflows through the Roche lobe and enters the gravitational field of the black hole [1]. Viscous interactions between adjacent gas layers in the accretion disk cause angular momentum to transfer from the rapidly rotating inner regions to the slower outer regions. The inner regions, having lost angular momentum, experience a reduction in centrifugal force and can no longer balance the gravitational pull, causing the inner material to fall toward the center. As the material falls into the black hole, the gravitational energy is converted to radiative energy, ultimately producing intense X-ray radiation and resulting in X-ray outbursts [2,3] .

The Hardness-Intensity Diagram (HID) is usually used to describe the state transitions of BH XRBs. A normal outburst typically undergoes four distinct states: the low hard state (LHS), the hard intermediate state (HIMS), the soft intermediate state (SIMS), and the high soft state (HSS) [4,5]. In the low hard state, the X-ray emissions are dominated by non-thermal radiation from the corona or the base of the jet [2,6]. The corona, composed of high-temperature and low-density plasma, usually locates above the accretion disk. In contrast, in the high soft state, the X-ray emissions are dominated by thermal radiation from the accretion disk, which has a higher temperature and emits mainly in the soft X-ray band [7]. The hard intermediate state and the soft intermediate state represent transitional phases between the low hard state and the high soft state [4,8]. In the hard intermediate state, the radiations from the corona remain strong, but the thermal radiation from the accretion disk begins to increase significantly. In the soft intermediate state, the thermal radiations from the accretion disk gradually become dominant, while the radiations from the corona are weakening [9].

 doi:10.20944/preprints202504.0693.v1

Quasi-Periodic Oscillations (QPOs) are universal timing phenomena observed in every BH XRBs, manifesting as nearly periodic fluctuations in the X-ray light curves [10]. The frequencies and characteristics of QPOs are closely related to the dynamical processes in the accretion disk, making them crucial to study the physical processes near black holes [11,12]. Based on their central frequencies, QPOs can be classified into high-frequency QPOs (HF QPOs, $\nu_{QPO} > 30Hz$) and low-frequency QPOs (LF QPOs, $\nu_{QPO} < 30Hz$) [13]. Based on their quality factor (Q-value), noise properties and relative RMS (root-mean-square) amplitude, LF QPOs can be further classfied into Type A, Type B, and Type C [14,15]. Among these, Type C QPOs usually exhibit high Q-values and significant broadband noise, while Type A and Type B QPOs have lower Q-values and distinct noise characteristics. Type C QPOs predominantly appear in the low hard state and hard intermediate state, potentially related to the dynamics of the corona or the jet. Type A and Type B QPOs are mainly observed in the soft intermediate state and may be associated with instabilities in the accretion disk or interactions between the corona and the disk[10]. In the high soft state, where the radiation from the accretion disk dominates, QPOs are generally not observed.To date, the origin of QPOs (quasi-periodic oscillations) remains an opening questions in astrophysics. Numerous models have been proposed to explore the physics under the QPO phenomena, such as the Lense-Thirring precession[16], the precessing inner flow model [11], corrugation modes [10], and accretion-ejection instability [17]. Among these, the Lense-Thirring precession model is widely used to explain Type C QPOs. The precessing implied that the QPOs are contributed from the precession of the inner region of the accretion disk, that are usually induced by the black hole's spin [18].

Swift J1727.8–1613 is a famous BH XRBs, which was first discovered by NASA's Swift satellite on August 24, 2023. Following its discovery, the object was observed by multiple space telescopes and ground-based instruments across the X-ray, radio, and optical bands, and through the analysis of observational data, it has been identified as a low-mass black hole X-ray binary [2]. It is reported that the source is located approximately 2.7 ± 0.3 kpc from Earth [19], with the black hole having a mass of about $10 \pm 2\ M_{\odot}$ [20]. During the outburst, significant Type C quasi-periodic oscillations (QPOs) were detected in the timing analysis of data from multiple space telescopes [21]. In particular, the Hard X-ray Modulation Telescope (Insight-HXMT) observations primarily revealed Type C QPOs in the frequency range of 0.1–8.0 Hz, providing crucial data for studying the dynamical processes around the black hole [22,23].

In this paper,the primary objective of this study is to explore the timing properties of Swift J1727.8-1613 during its 2023 outburst, with particular focus on the evolution of quasi-periodic oscillations (QPOs). The paper is organized as follows: Section 2 describes the observations and data reduction procedures. Section 3 details our timing analysis methodology, including QPO characterization and power spectral modeling. Section 4 discusses the physical implications of our results in the context of accretion disk dynamics and black hole physics.

2. Observations and Data Reduction

Insight-HXMT, China's first X-ray astronomy satellite, was successfully launched on June 15, 2017 [24–26] . Equipped with three scientific payloads, the satellite covers a broad energy range from 1 - 250 keV, enabling comprehensive observations of high-energy astrophysical phenomena. The Low-Energy X-ray Telescope (LE) utilizes swept charge device (SCD) detectors to observe in the 1–15 keV range, with a total geometrical area of 384 cm^2 [27]. The Medium-Energy X-ray Telescope (ME) employs Si-PIN detectors, operating in the 5–35 keV band and features a geometrical area of 952 cm^2 [28]. The High-Energy X-ray Telescope (HE), based on phoswich NaI(CsI) detectors, covers the 20–250 keV range with a total geometrical area of 5100 cm^2 [29]. Together, these instruments allow Insight-HXMT to study a variety of X-ray sources, including black holes, neutron stars, and gamma-ray bursts, providing valuable insights into the high-energy processes governing these objects.

The observations of Swift J1727.8–1613 from the Insight-HXMT spanned from August 25, 2023, to October 6, 2023, comprising a total of 34 independent observation sessions. In this study, we initially

 doi:10.20944/preprints202504.0693.v1

selected the first ten available observation IDs, comprising 104 exposures in total. However, quasi-periodic oscillations (QPOs) were only detected in 99 of these exposures. Detailed information on the selected data is provided in Table 1. In Figure 1, we present the light curve and hardness-intensity diagram (HID) for the LE (2–10 keV) band. From the light curve, it can be seen that the count rate of LE band rapidly increased from approximately 1250 counts/s to around 3250 counts/s. The count rate peaked near MJD 60186 and then began to decline gradually. The hardness-intensity diagram indicates that the source was in a transitional state between the low hard state and the hard intermediate state during this period.

Table 1. The results of timing analysis of Swift J1727.8-1613.

Exposure ID	Start MJD	Exposure Time(s)	QPO Frequency (Hz)	RMS	Q-value
P61433800108	60182.28	2504	$0.242^{+0.005}_{-0.005}$	$11.172^{+0.777}_{-1.235}$	6^{+3}_{-2}
P61433800109	60182.41	2240	$0.285^{+0.003}_{-0.003}$	$12.343^{+0.895}_{-0.541}$	6^{+4}_{-2}
P61433800110	60182.55	2670	$0.303^{+0.003}_{-0.003}$	$11.777^{+0.314}_{-0.296}$	7^{+4}_{-3}
P61433800111	60182.68	1290	$0.339^{+0.010}_{-0.011}$	$14.380^{+0.195}_{-0.175}$	6^{+3}_{-3}
P61433800112	60182.81	1118	$0.369^{+0.005}_{-0.006}$	$13.385^{+0.228}_{-0.267}$	9^{+5}_{-4}
P61433800201	60183.05	164.6	$0.430^{+0.026}_{-0.029}$	$13.413^{+0.801}_{-1.077}$	7^{+4}_{-3}
P61433800202	60183.20	2784	$0.450^{+0.004}_{-0.004}$	$13.024^{+0.153}_{-0.146}$	11^{+6}_{-5}
P61433800203	60183.34	1775	$0.496^{+0.010}_{-0.009}$	$16.485^{+0.374}_{-0.344}$	4^{+2}_{-2}
P61433800204	60183.48	2453	$0.511^{+0.007}_{-0.007}$	$13.562^{+0.066}_{-0.075}$	9^{+5}_{-4}
P61433800205	60183.61	119.7	$0.484^{+0.026}_{-0.016}$	$13.032^{+0.110}_{-0.118}$	30^{+18}_{-10}
P61433800206	60183.74	527.7	$0.593^{+0.011}_{-0.012}$	$14.994^{+0.314}_{-0.301}$	4^{+2}_{-2}
P61433800207	60183.87	418.9	$0.598^{+0.010}_{-0.009}$	$12.617^{+0.949}_{-1.360}$	22^{+11}_{-10}
P61433800208	60184.00	359.1	$0.638^{+0.013}_{-0.024}$	$13.458^{+0.163}_{-0.177}$	15^{+8}_{-7}
P61433800209	60184.14	2034	$0.680^{+0.008}_{-0.009}$	$14.629^{+0.164}_{-0.166}$	8^{+4}_{-4}
P61433800210	60184.26	2271	$0.706^{+0.007}_{-0.007}$	$14.080^{+0.492}_{-0.489}$	9^{+5}_{-4}
P61433800211	60184.40	2095	$0.705^{+0.008}_{-0.008}$	$14.956^{+0.189}_{-0.231}$	6^{+3}_{-3}
P61433800212	60184.53	1727	$0.713^{+0.009}_{-0.009}$	$14.658^{+0.153}_{-0.151}$	9^{+4}_{-4}
P61433800301	60185.30	3292	$0.888^{+0.005}_{-0.005}$	$14.573^{+0.099}_{-0.109}$	8^{+4}_{-4}
P61433800302	60185.46	2555	$0.878^{+0.010}_{-0.009}$	$14.109^{+0.133}_{-0.138}$	9^{+5}_{-4}
P61433800303	60185.59	2691	$0.814^{+0.008}_{-0.009}$	$13.215^{+0.110}_{-0.140}$	11^{+6}_{-5}
P61433800304	60185.72	2118	$0.864^{+0.012}_{-0.016}$	$14.142^{+0.360}_{-0.335}$	5^{+3}_{-3}
P61433800305	60185.85	359.1	$0.979^{+0.019}_{-0.023}$	$14.645^{+0.188}_{-0.158}$	7^{+4}_{-3}
P61433800306	60185.99	435.9	$1.107^{+0.031}_{-0.000}$	$12.902^{-0.001}_{-0.247}$	10^{+5}_{-5}
P61433800307	60186.12	2753	$1.065^{+0.005}_{-0.006}$	$15.031^{+0.642}_{-0.694}$	7^{+4}_{-3}
P61433800308	60186.24	2394	$1.129^{+0.011}_{-0.011}$	$13.859^{+0.165}_{-0.193}$	9^{+5}_{-4}
P61433800309	60186.38	2366	$1.126^{+0.008}_{-0.009}$	$13.402^{+0.307}_{-0.343}$	8^{+4}_{-4}
P61433800310	60186.51	2006	$1.133^{+0.011}_{-0.012}$	$13.916^{+0.429}_{-0.480}$	8^{+4}_{-4}
P61433800311	60186.65	2514	$1.146^{+0.009}_{-0.008}$	$14.339^{+0.214}_{-0.266}$	8^{+4}_{-4}
P61433800312	60186.78	179.5	$1.286^{+0.039}_{-0.032}$	$13.333^{+0.656}_{-0.750}$	14^{+7}_{-7}
P61433800314	60187.04	1473	$1.078^{+0.009}_{-0.008}$	$13.229^{+0.284}_{-0.331}$	10^{+6}_{-4}
P61433800401	60187.15	2152	$1.156^{+0.010}_{-0.010}$	$14.044^{+0.151}_{-0.167}$	9^{+5}_{-4}
P61433800402	60187.30	2423	$1.140^{+0.008}_{-0.008}$	$14.145^{+0.133}_{-0.161}$	8^{+4}_{-4}
P61433800403	60187.44	359.1	$1.266^{+0.015}_{-0.015}$	$13.416^{+0.357}_{-0.444}$	13^{+7}_{-6}
P61433800404	60187.57	943.6	$1.127^{+0.017}_{-0.018}$	$13.806^{+0.115}_{-0.062}$	7^{+4}_{-3}
P61433800405	60187.70	1910	$1.169^{+0.013}_{-0.013}$	$13.435^{+0.326}_{-0.261}$	8^{+4}_{-4}
P61433800407	60187.97	777.1	$1.329^{+0.021}_{-0.023}$	$13.807^{+0.613}_{-0.693}$	8^{+4}_{-4}
P61433800408	60188.10	2493	$1.335^{+0.011}_{-0.013}$	$13.642^{+0.166}_{-0.168}$	9^{+4}_{-4}
P61433800409	60188.22	1017	$1.197^{+0.017}_{-0.014}$	$12.867^{+0.387}_{-0.410}$	7^{+4}_{-3}
P61433800410	60188.36	2419	$1.205^{+0.011}_{-0.012}$	$13.787^{+0.202}_{-0.217}$	8^{+4}_{-4}
P61433800411	60188.50	1796	$1.178^{+0.006}_{-0.006}$	$12.438^{+0.145}_{-0.102}$	9^{+5}_{-4}
P61433800412	60188.63	463.8	$1.213^{+0.026}_{-0.022}$	$13.552^{+0.988}_{-1.055}$	9^{+5}_{-5}
P61433800413	60188.76	778.1	$1.232^{+0.014}_{-0.015}$	$14.098^{+0.353}_{-0.452}$	8^{+4}_{-4}
P61433800414	60188.89	920.7	$1.237^{+0.018}_{-0.018}$	$13.391^{+0.247}_{-0.212}$	8^{+4}_{-4}
P61433800501	60189.07	3148	$1.313^{+0.011}_{-0.009}$	$13.680^{+0.154}_{-0.151}$	8^{+4}_{-4}
P61433800502	60189.22	1179	$1.355^{+0.016}_{-0.015}$	$12.743^{+0.617}_{-0.723}$	11^{+6}_{-5}
P61433800503	60189.35	2274	$1.237^{+0.010}_{-0.010}$	$12.672^{+0.313}_{-0.323}$	8^{+4}_{-4}
P61433800504	60189.49	2019	$1.168^{+0.001}_{-0.010}$	$12.918^{+0.606}_{-0.026}$	9^{+5}_{-5}
P61433800505	60189.62	2329	$1.243^{+0.020}_{-0.022}$	$13.872^{+0.007}_{-0.008}$	5^{+2}_{-2}
P61433800506	60189.75	718.2	$1.352^{+0.021}_{-0.022}$	$13.135^{+0.326}_{-0.422}$	7^{+4}_{-4}
P61433800507	60189.88	225.4	$1.337^{+0.030}_{-0.036}$	$12.844^{+1.574}_{-1.825}$	10^{+5}_{-5}
P61433800508	60190.02	2214	$1.450^{+0.013}_{-0.011}$	$13.469^{+0.106}_{-0.123}$	7^{+4}_{-3}
P61433800509	60190.15	1013	$1.335^{+0.017}_{-0.015}$	$13.748^{+0.043}_{-0.031}$	9^{+5}_{-4}
P61433800511	60190.41	1197	$1.280^{+0.013}_{-0.011}$	$12.488^{+0.123}_{-0.143}$	11^{+6}_{-5}
P61433800512	60190.54	2029	$1.296^{+0.011}_{-0.011}$	$12.542^{+0.000}_{-0.000}$	8^{+4}_{-4}
P61433800513	60190.68	1717	$1.309^{+0.014}_{-0.013}$	$13.229^{+0.165}_{-0.164}$	9^{+4}_{-4}
P61433800515	60190.94	1421	$1.234^{+0.012}_{-0.013}$	$13.074^{+0.611}_{-0.599}$	8^{+4}_{-4}
P61433800601	60191.06	3231	$1.250^{+0.008}_{-0.008}$	$13.260^{+0.445}_{-0.460}$	7^{+4}_{-3}

 doi:10.20944/preprints202504.0693.v1

Table 1. data of radiatively efficient AGNs (continued).

Exposure ID	Start MJD	Exposure Time(s)	QPO Frequency (Hz)	RMS	Q-value
P61433800602	60191.20	2191	$1.182^{+0.012}_{-0.012}$	$12.603^{+0.353}_{-0.303}$	8^{+4}_{-4}
P61433800603	60191.34	2153	$1.135^{+0.013}_{-0.012}$	$13.660^{+0.244}_{-0.220}$	6^{+3}_{-3}
P61433800604	60191.47	1712	$1.176^{+0.015}_{-0.015}$	$12.669^{+0.341}_{-0.343}$	10^{+5}_{-5}
P61433800605	60191.60	1463	$1.081^{+0.014}_{-0.014}$	$12.751^{+0.001}_{-0.001}$	8^{+4}_{-4}
P61433800606	60191.73	538.7	$1.070^{+0.004}_{-0.004}$	$13.409^{+0.608}_{-0.700}$	6^{+4}_{-2}
P61433800607	60191.87	359.1	$1.154^{+0.019}_{-0.014}$	$11.524^{+0.393}_{-0.266}$	10^{+5}_{-5}
P61433800608	60192.00	2394	$1.122^{+0.009}_{-0.008}$	$12.791^{+0.422}_{-0.129}$	8^{+4}_{-4}
P61433800611	60192.39	1855	$1.531^{+0.024}_{-0.024}$	$12.844^{+0.261}_{-0.360}$	5^{+3}_{-3}
P61433800612	60192.53	1736	$1.460^{+0.017}_{-0.016}$	$12.653^{+0.553}_{-0.621}$	7^{+4}_{-3}
P61433800613	60192.66	1666	$1.378^{+0.012}_{-0.011}$	$12.787^{+0.319}_{-0.327}$	9^{+5}_{-5}
P61433800615	60192.92	1377	$1.458^{+0.012}_{-0.014}$	$12.470^{+0.518}_{-0.575}$	9^{+5}_{-4}
P61433800616	60193.06	2734	$1.463^{+0.013}_{-0.013}$	$12.785^{+0.277}_{-0.271}$	8^{+4}_{-4}
P61433800617	60193.19	1436	$1.401^{+0.011}_{-0.011}$	$12.212^{+0.081}_{-0.075}$	8^{+4}_{-4}
P61433800618	60193.32	1774	$1.359^{+0.016}_{-0.016}$	$12.965^{+0.165}_{-0.139}$	7^{+3}_{-3}
P61433800801	60194.03	2753	$1.299^{+0.011}_{-0.010}$	$14.036^{+0.084}_{-0.082}$	4^{+2}_{-2}
P61433800802	60194.17	1878	$1.299^{+0.012}_{-0.011}$	$12.705^{+0.259}_{-0.279}$	7^{+3}_{-3}
P61433800803	60194.31	1496	$1.400^{+0.015}_{-0.014}$	$12.766^{+0.098}_{-0.097}$	8^{+4}_{-4}
P61433800804	60194.44	1496	$1.491^{+0.020}_{-0.022}$	$12.485^{+0.143}_{-0.143}$	6^{+3}_{-3}
P61433800805	60194.71	1407	$1.664^{+0.010}_{-0.011}$	$12.464^{+0.223}_{-0.235}$	8^{+4}_{-4}
P61433800807	60194.84	335.2	$1.446^{+0.033}_{-0.037}$	$11.322^{+0.109}_{-0.216}$	8^{+4}_{-4}
P61433800808	60194.97	2392	$1.300^{+0.011}_{-0.011}$	$12.643^{+0.001}_{-0.000}$	7^{+4}_{-3}
P61433800901	60195.09	1975	$1.312^{+0.019}_{-0.018}$	$12.562^{+0.000}_{-0.000}$	6^{+3}_{-3}
P61433800902	60195.23	1609	$1.387^{+0.012}_{-0.011}$	$11.785^{+0.215}_{-0.194}$	9^{+5}_{-4}
P61433800903	60195.37	1541	$1.406^{+0.014}_{-0.016}$	$11.718^{+0.234}_{-0.276}$	8^{+6}_{-3}
P61433800904	60195.50	1458	$1.306^{+0.013}_{-0.013}$	$11.932^{+0.311}_{-0.352}$	9^{+5}_{-4}
P61433800905	60195.63	538.7	$1.368^{+0.017}_{-0.018}$	$11.281^{+0.337}_{-0.372}$	11^{+6}_{-5}
P61433800906	60195.76	114.7	$1.565^{+0.046}_{-0.053}$	$12.367^{+0.375}_{-0.724}$	5^{+3}_{-2}
P61433800907	60195.90	2748	$1.394^{+0.007}_{-0.009}$	$11.773^{+0.207}_{-0.250}$	8^{+4}_{-4}
P61433801001	60196.08	1938	$1.384^{+0.008}_{-0.007}$	$11.987^{+0.207}_{-0.217}$	9^{+4}_{-4}
P61433801002	60196.22	1652	$1.265^{+0.015}_{-0.013}$	$11.346^{+0.462}_{-0.542}$	8^{+4}_{-4}
P61433801003	60196.36	1604	$1.222^{+0.017}_{-0.015}$	$11.410^{+0.269}_{-0.305}$	8^{+4}_{-4}
P61433801004	60196.49	1255	$1.127^{+0.015}_{-0.014}$	$12.031^{+0.091}_{-0.109}$	9^{+4}_{-4}
P61433801005	60196.62	299.2	$1.093^{+0.012}_{-0.018}$	$12.650^{+0.179}_{-0.011}$	9^{+5}_{-4}
P61433801006	60196.76	167.6	$1.195^{+0.019}_{-0.016}$	$9.162^{+1.139}_{-0.832}$	21^{+12}_{-9}
P61433801007	60196.89	2936	$1.303^{+0.012}_{-0.011}$	$12.107^{+0.141}_{-0.116}$	7^{+4}_{-3}
P61433801101	60197.07	1842	$1.463^{+0.014}_{-0.015}$	$11.543^{+0.117}_{-0.158}$	9^{+5}_{-4}
P61433801102	60197.21	1496	$1.502^{+0.009}_{-0.009}$	$10.695^{+0.180}_{-0.200}$	11^{+6}_{-5}
P61433801103	60197.35	1768	$1.432^{+0.013}_{-0.015}$	$11.714^{+0.089}_{-0.103}$	8^{+4}_{-4}
P61433801104	60197.48	1287	$1.443^{+0.016}_{-0.018}$	$11.156^{+0.131}_{-0.112}$	10^{+5}_{-5}
P61433801105	60197.62	239.4	$1.427^{+0.062}_{-0.045}$	$11.434^{+0.401}_{-0.448}$	7^{+4}_{-3}
P61433801106	60197.75	239.4	$1.653^{+0.027}_{-0.026}$	$9.607^{+0.304}_{-0.408}$	11^{+5}_{-5}
P61433801107	60197.88	2022	$1.847^{+0.011}_{-0.010}$	$11.082^{+0.222}_{-0.217}$	9^{+5}_{-4}

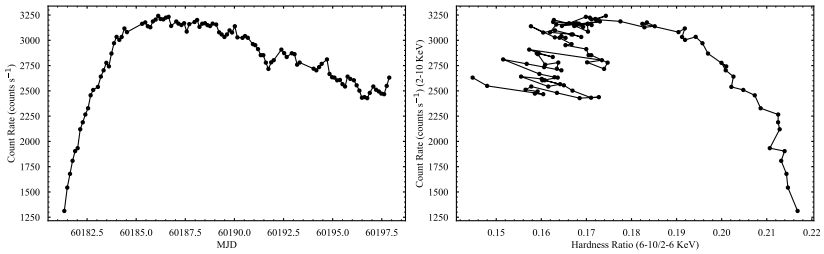

Figure 1. The Light curve and hardness-intensity diagram (HID) of Swift J1727.8-1613.

The data from the Low-Energy X-ray Telescope (LE) were processed using the Insight-HXMT Data Analysis Software `HXMTDAS v2.06` [1]. To ensure data quality, standard filtering criteria were applied: the pointing offset angle was restricted to less than 0°.04, the Earth elevation angle was required to exceed 10°, and the geomagnetic cutoff rigidity was set to values greater than 8 GV. Additionally, data were excluded within 300 seconds before and after the satellite's passage through the South Atlantic Anomaly. These criteria were implemented to minimize background contamination and ensure the reliability of the LE data for subsequent analysis.

[1] http://hxmtweb.ihep.ac.cn/software.jhtml

 doi:10.20944/preprints202504.0693.v1

3. Data Analysis and Results

To investigate the timing properties of Swift J1727.8–1613, we generated light curves with a time resolution of 1/128s. The power density spectrum (PDS) was computed with the fast Fourier transform (FFT) method, which was implemented through the `powspec` task in the `XRONOS` package in the `HEASoft` software. For each exposure, the data were divided into multiple segments, each containing 8192 new bins to ensure sufficient resolution. Firstly, the PDS was calculated for each individual data segment, and then the resulting PDS values were averaged to generate the final composite PDS. The PDS normalization was performed such that its integral represents the fractional root mean square variability. To mitigate the impact of white noise, a normalization factor of -2 was applied in the `powspec` task, and a geometric rebinning factor of -1.03 was used to enhance spectral resolution. The PDS was converted into an energy spectrum format, and both the QPO and broadband noise were fitted using a Lorentzian function within `Xspec`. The form of the Lorentzian function is as follows [10]:

$$L(\nu) = \frac{a_0^2}{\pi/2 + \arctan(\nu_0/\Delta)} \cdot \frac{\Delta}{\Delta^2 + (\nu - \nu_0)^2} \tag{1}$$

where ν denotes the Fourier frequency, ν_0 represents the centroid frequency of the quasi-periodic oscillation (QPO), Δ corresponds to the half width at half maximum, and a_0^2 is the total power obtained by integrating $L(\nu)$ over all frequencies ($0 \leq \nu < \infty$). Through spectral fitting, we have derived the central frequency of QPO, full width at half maximum (FWHM), and root mean square amplitude (RMS) for each observational exposure, as summarized in Table 1. The quality factor Q is defined as $Q = \nu_0/(2\Delta)$ (see Table 1). Figure 2 shows the evolution of the QPO frequency of Swift J1727.8-1613. Several time points from MJD=60182 to MJD=60198 are marked in the figure, illustrating the evolution of the QPO frequency during different observational periods. As illustrated in Figure 2, it can be seen that the QPO frequency exhibited a significant rising trend at MJD=60182-60186, increasing from approximately 0.2 Hz to 1.2 Hz. Then, the QPO frequency remained stable around 1.2 Hz at MJD=60186 - 60190. Starting from MJD=60190, the QPO frequency gradually decreased, reaching 1.0 Hz at MJD=60192. Afterward, there was an alternating pattern of increases and decreases, with the frequency eventually reaching about 1.8 Hz. This process of rising, stabilizing, and falling frequencies may be related to changes in the radius of the accretion disk or adjustments in the accretion rate. The figure provides a clear observation of the dynamic variation of the QPO frequency over time, offering valuable information for studying the dynamical processes of black hole accretion disks, such as the evolution of the accretion disk radius and the geometric structure of the corona. Figure 3 shows the evolution of the RMS amplitude of the QPO. From the figure, it can be found that the RMS values remains stable and stays around 0.14 between MJD 60182 and MJD 60190. Starting from MJD 60190, the RMS values gradually decreased, reaching about 0.10 at MJD=60198. Figure 4 displays the Power Density Spectra (PDS) and their fitting residuals for six exposures in chronological order, showcasing the fitting results for the QPO and broadband noise.

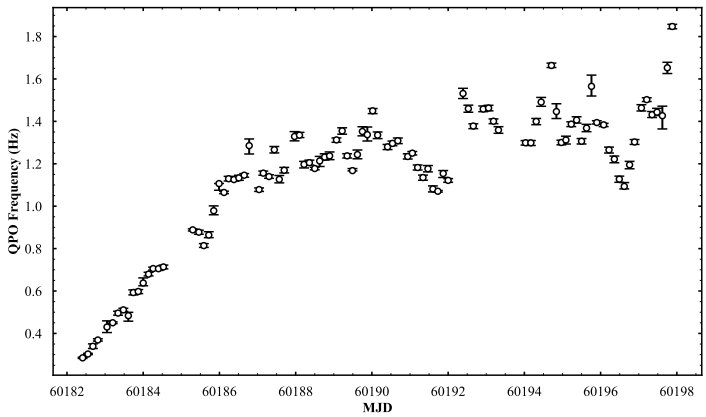

Figure 2. The evolution of the quasi-periodic oscillation (QPO) frequency of Swift J1727.8-1613.

 doi:10.20944/preprints202504.0693.v1

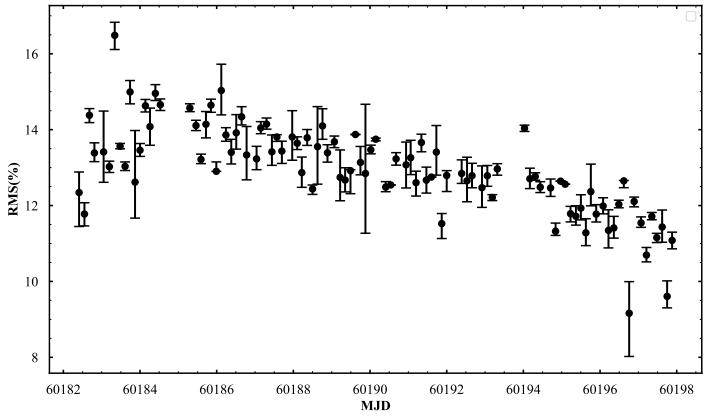

Figure 3. The evolution of the root mean square (RMS) of the QPO in Swift J1727.8-1613.

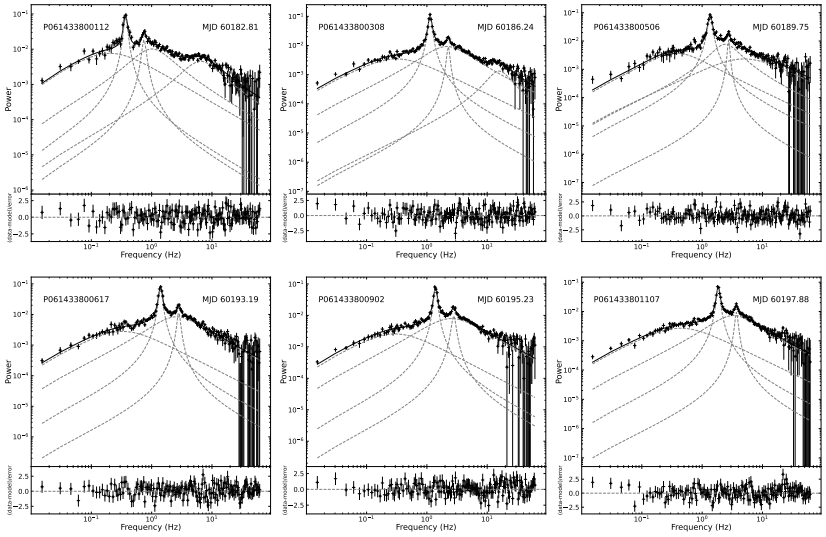

Figure 4. The six power density spectra of Swift J1727.8-1613.

4. Discussion and Conclusion

Our study of the black hole X-ray binary Swift J1727.8–1613 has revealed significant insights into its accretion dynamics and quasi-periodic oscillation (QPO) behavior during its 2023 outburst. Using data from Insight-HXMT, we tracked the source's timing properties across multiple epochs. The light curve in the 2–10 keV band exhibited a rapid rise in count rate from 1250 to 3250 counts/s, peaking around MJD 60186 before gradually declining (see Figure 1). The hardness-intensity diagram (HID) indicated a transition from the low hard state (LHS) to the hard intermediate state (HIMS), marked by a decrease in hardness ratio from 0.22 to 0.15. Timing analysis revealed strong Type C QPOs with frequencies evolving from 0.2 Hz to 1.8 Hz, accompanied by stable fractional RMS ($\sim$ 14%) in the initial phase, followed by a decline to $\sim$ 10% (see Figures 2 and Figure 3). According to the classification criteria for low-frequency QPOs, we have classified all the detected QPOs as Type C QPOs. Chatterjee et al. (2024) also conducted timing analysis on the first ten observation IDs (totaling 92 exposures) of Swift J1727.8-1613, identifying QPOs in the frequency range of 0.21 $\pm$ 0.01 - 1.86 $\pm$ 0.01 Hz, which they similarly classified as Type C QPOs - consistent with our findings [30–32]. In this work, we suggest that the observed frequency evolution matches the predictions of the Lense-Thirring (L-T) precession model, which attributes Type C QPOs to relativistic frame-dragging effects near a spinning black hole [e.g., [12,33–36]]. This model operates under the assumption of a truncated disk configuration. As the accretion rate rises, the inner boundary of the accretion disk moves inward, consequently driving an increase in the precession frequency. Here, the precession frequency $\nu_{\rm LT}$ can be expressed as [11]:

 doi:10.20944/preprints202504.0693.v1

$$\nu_\phi = \frac{c}{2\pi R_g \left(r^{3/2} + a\right)} \tag{2}$$

$$\nu_{\rm LT} = \nu_\phi \left(1 - \sqrt{1 - \frac{4a}{r^{3/2}} + \frac{3a^2}{r^2}}\right) \tag{3}$$

where a represents the dimensionless spin parameter ($-1 < a < 1$), and r denotes the orbital radius normalized by the gravitational radius $R_g = GM/c^2$. A significant inverse correlation between the coronal truncation radius and low-frequency QPO (LFQPO) frequency demonstrates both qualitative and quantitative consistency with the Lense-Thirring precession model originally proposed by [11,37–39]. The observational data indicate that the source is undergoing a transition from the low hard state (LHS) to the hard intermediate state (HIMS). As the accretion rate increases, the inner radius of the accretion disk is expected to decrease. According to the relationship between the L-T precession frequency and the inner disk radius given by Eq.3, this reduction in inner radius should directly lead to an increase in the precession frequency. This prediction is fully consistent with the evolution of QPO frequencies shown in Figure 2. On the other hand, during the initial transition phase from the low hard state (LHS) to the hard intermediate state (HIMS), the inner radius of the accretion disk remains relatively large. At this stage, the corona structure is geometrically thick and located farther from the black hole. Its precession induces continuous variation in the line-of-sight angle of X-ray emission. Due to the intrinsic anisotropy of coronal radiation, the observed flux exhibits periodic modulation, contributing to the higher RMS values. As the accretion rate increases and the inner disk radius contracts, the vertical extent of the corona diminishes, consequently reducing the amplitude of precession-induced flux modulation - i.e., leading to decreased RMS. This physical picture corresponds well with the evolution of RMS shown in Figure 3.

Author Contributions: Conceptualization, Ai-Jun Dong; methodology, Yi, Wen and Ai-Jun Dong; Software, Yi Wen and Chao Huang; Investigation, Ai-Jun, Dong and Yi, Wen; writing-original draft preparation, Yi Wen and Ai-Jun Dong. All authors have read and agreed to the published version of the manuscript.

Funding: This work is supported by the NSFC (12363005), the National SKA Program of China (2022SKA0130104), the Foundation of Guizhou Provincial Education Department ((2020)0030), the Scientific Research Project of the Guizhou Provincial Education (KY[2022]132, KY[2022]137), Major Science and Technology Program of Xinjiang Uygur Autonomous Region (2022A03013-4) and Projects of the Grassroots Science Popularization Action Plan of Guizhou Provincial Association for Science and Technology.

Institutional Review Board Statement: Not applicable.

Informed Consent Statement: Not applicable.

Data Availability Statement: Not applicable.

Conflicts of Interest: The authors declare no conflict of interest.

References

1. Shakura, N. I.; Sunyaev, R. A.. Black holes in binary systems. Observational appearance. *Astron. Astrophys.* **1973**, *24*, 337.
2. Peng, J.-Q.; Zhang, S.; Shui, Q.-C.; Zhang, S.-N.; Kong, L.-D.; Chen, Y.-P.; et al.. NICER, NuSTAR, and Insight-HXMT views to the newly discovered black hole X-ray binary Swift J1727.8-1613. *Astrophys. J. Lett.* **2024**, *960*, 17.
3. Lasota, J.P.. The disc instability model of dwarf novae and low-mass X-ray binary transients. *New Astron. Rev.* **2001**, *45*, 449.
4. Belloni, T.; Homan, J.; Casella, P.; van der Klis, M.; Nespoli, E.; Lewin, W.H.G.; et al.. The evolution of the timing properties of the black-hole transient GX 339–4 during its 2002/2003 outburst. *Astron. Astrophys.* **2005**, *440*, 207.
5. Motta, S.; Belloni, T.; Homan, J.. The evolution of the high-energy cut-off in the X-ray spectrum of GX 339–4 across a hard-to-soft transition. *Mon. Not. R. Astron. Soc.* **2009**, *400*, 1603.

 doi:10.20944/preprints202504.0693.v1

6. Reig, P.; Kylafis, N.. The origin of the hard X-ray tail in neutron-star X-ray binaries. *Astron. Astrophys.* **2016**, *591*, 24.
7. McClintock, J.E.; Remillard, R.A.. Black hole binaries. In *Compact stellar X-ray sources*; Lewin, W.H.G.; van der Klis, M., Eds.; Cambridge University Press: Cambridge, UK, **2006**, *39*, 157.
8. Homan, J.; Belloni, T.. The Evolution of Black Hole States. *Astrophys. Space Sci.* **2005**, *300*(1-3), 107.
9. Peng, J.-Q.; Zhang, S.; Shui, Q.-C.; Chen, Y.-P.; Zhang, S.-N.; Kong, L.-D.; et al.. Insight-HXMT, NICER, and NuSTAR Views to the Newly Discovered Black Hole X-Ray Binary Swift J151857.0 –572147. *Astrophys. J. Lett.* **2024**, *973*(1), 7.
10. Ingram, A.R.; Motta, S.E.. A review of quasi-periodic oscillations from black hole X-ray binaries: Observation and theory. *New Astron. Rev.* **2019**, *85*, 101524.
11. Ingram, A.; Done, C.; Fragile, P.C.. Low-frequency quasi-periodic oscillations spectra and Lense-Thirring precession. *Mon. Not. R. Astron. Soc.* **2009**, *397*(1), 101.
12. Ma, X.; Zhang, L.; Tao, L.; Bu, Q.C.; Qu, J.L.; Zhang, S.N.; et al.. A Detailed View of Low-frequency Quasi-periodic Oscillation in the Broadband 0.2-200 keV with Insight-HXMT and NICER. *Astrophys. J.* **2023**, *948*(2), 116.
13. Belloni, T.M.. States and Transitions in Black Hole Binaries. In *Lecture Notes in Physics, Berlin Springer Verlag*; Belloni, T., Ed.; Springer: Berlin, Germany, **2010**, *794*, 53.
14. Wijnands, R.; Homan, J.; van der Klis, M.. The Complex Phase-Lag Behavior of the 3-12 Hz Quasi-Periodic Oscillations during the Very High State of XTE J1550-564. *Astrophys. J. Lett.* **1999**, *526*(1), 33.
15. Casella, P.; Belloni, T.; Stella, L.. The ABC of Low-Frequency Quasi-periodic Oscillations in Black Hole Candidates: Analogies with Z Sources. *Astrophys. J.* **2005**, *629*(1), 403.
16. Stella, L.; Vietri, M.. Lense-Thirring Precession and Quasi-periodic Oscillations in Low-Mass X-Ray Binaries. *Astrophys. J. Lett.* **1998**, *492*(1), 59.
17. Tagger, M.; Pellat, R.. An accretion-ejection instability in magnetized disks. *Astron. Astrophys.* **1999**, *349*, 1003.
18. Shui, Q.C.; Zhang, S.; Chen, Y.P.; Zhang, S.N.; Kong, L.D.; Wang, P.J.; et al.. Tracing the Accretion Geometry of H1743-322 with Type C Quasiperiodic Oscillations in Multiple Outbursts. *Astrophys. J.* **2023**, *943*(2), 165.
19. Mata Sánchez, D.; Muñoz-Darias, T.; Armas Padilla, M.; Casares, J.; Torres, M.A.P.. Evidence for inflows and outflows in the nearby black hole transient Swift J1727.8−162. *Astron. Astrophys.* **2024**, *682*, 1.
20. Svoboda, J.; Dovčiak, M.; Steiner, J.F.; Kaaret, P.; Podgorný, J.; Poutanen, J.; et al.. Dramatic Drop in the X-Ray Polarization of Swift J1727.8–1613 in the Soft Spectral State. *Astrophys. J. Lett.* **2024**, *966*(2), 35.
21. Shui, Q.-C.; Zhang, S.; Peng, J.-Q.; Zhang, S.-N.; Chen, Y.-P.; Ji, L.; et al.. Phase-resolved Spectroscopy of Low-frequency Quasiperiodic Oscillations from the Newly Discovered Black Hole X-Ray Binary Swift J1727.8-1613. *Astrophys. J.* **2024**, *973*(1), 59.
22. Yu, W.; Bu, Q.-C.; Zhang, S.-N.; Liu, H.-X.; Zhang, L.; Ducci, L.; et al.. Timing analysis of the newly discovered black hole candidate Swift J1727.8-1613 with Insight-HXMT. *Mon. Not. R. Astron. Soc.* **2024**, *529*(4), 4624.
23. Zhu, H.; Wang, W.. Energy Dependence of the Low-frequency Quasiperiodic Oscillations in Swift J1727.8 –1613. *Astrophys. J.* **2024**, *968*(2), 106.
24. Zhang, S.; Lu, F.J.; Zhang, S.N.; Li, T.P.. Introduction to the hard x-ray modulation telescope. In *Space Telescopes and Instrumentation 2014: Ultraviolet to Gamma Ray*; Takahashi, T.; den Herder, J.-W.A.; Bautz, M., Eds.; Society of Photo-Optical Instrumentation Engineers (SPIE) Conference Series, **2014**, *9144*, 914421.
25. Zhang, S.; Zhang, S.N.; Lu, F.J.; Li, T.P.; Song, L.M.; Xu, Y.P.; et al.. The insight-HXMT mission and its recent progresses. In *Space Telescopes and Instrumentation 2018: Ultraviolet to Gamma Ray*; den Herder, J.-W.A.; Nikzad, S.; Nakazawa, K., Eds.; Society of Photo-Optical Instrumentation Engineers (SPIE) Conference Series, **2018**, *10699*, 106991U.
26. Zhang, S.-N.; Li, T.-P.; Lu, F.-J.; Song, L.-M.; Xu, Y.-P.; Liu, C.-Z.; et al. Overview to the Hard X-ray Modulation Telescope (Insight-HXMT) Satellite. *Sci. China Phys. Mech. Astron.* **2020**, *63*(4), 249502.
27. Chen, Y.; Cui, W.-W.; Li, W.; Wang, J.; Xu, Y.-P.; Lu, F.-J.; et al. The Low Energy X-ray telescope (LE) onboard the Insight-HXMT astronomy satellite. *Sci. China Phys. Mech. Astron.* **2020**, *63*(4), 249505.
28. Cao, X.; Jiang, W.; Meng, B.; Zhang, W.; Luo, T.; Yang, S.; et al.. The Medium Energy X-ray telescope (ME) onboard the Insight-HXMT astronomy satellite. *Sci. China Phys. Mech. Astron.* **2020**, *63*(4), 249504.
29. Liu, C.-Z.; Zhang, Y.-F.; Li, X.-F.; Lu, X.-F.; Chang, Z.; Li, Z.-W.; et al. The High Energy X-ray telescope (HE) onboard the Insight-HXMT astronomy satellite. *Sci. China Phys. Mech. Astron.* **2020**, *63*(4), 249503.
30. Chatterjee, K.; Mondal, S.; Singh, C. B.; Sugizaki, M.. Insight-HXMT View of the Black Hole Candidate Swift J1727.8–1613 during Its Outburst in 2023. *Astrophys. J.* **2024**, *977*(2), 148.

 doi:10.20944/preprints202504.0693.v1

31. Long, Q. C.; Dong, A. J.; Zhi, Q. J.; Shang, L. H., Revisiting the Fundamental Planes of Black Hole Activity for Strong Jet Sources. *Astrophys. J.*, **2025**, *980*(2), 187.
32. Dong, A. J.; Wu, Q. and Cao, X. F., A New Fundamental Plane for Radiatively Efficient Black-hole Sources, *Astrophys. J. lett.*, **2014**, *787*(2), 20.
33. Dong, A. J. and Liu, C.; Ge, K.; Liu, X. and Zhi, Q. J. and You, Z. Y., A study on the hysteresis effect and spectral evolution in the mini-outbursts of balck hole X-ray binary XTE J1550-564. Front. Astron. Space Sci, **2021**, *8*, 37.
34. Ingram, A.; van der Klis, M.; Middleton, M.; Done, C.; Altamirano, D.; Heil, L.; et al. A quasi-periodic modulation of the iron line centroid energy in the black hole binary H1743−322. *Mon. Not. R. Astron. Soc.* **2016**, *461*(2), 1967–1980.
35. Zhang, L.; Wang, Y.; Méndez, M.; Chen, L.; Qu, J.; Altamirano, D.; Belloni, T.. The Evolution of the Phase Lags Associated with the Type-C Quasi-periodic Oscillation in GX 339-4 during the 2006/2007 Outburst. *Astrophys. J.* **2017**, *845*(2), 143.
36. Huang, Y.; Qu, J. L.; Zhang, S. N.; Bu, Q. C.; Chen, Y. P.; Tao, L.; et al.. INSIGHT-HXMT Observations of the New Black Hole Candidate MAXI J1535−571: Timing Analysis. *Astrophys. J.* **2018**, *866*(2), 122.
37. Kubota, A.; Done, C.; Tsurumi, K.; Mizukawa, R.. Disc corona radii and QPO frequencies in black hole binaries: testing Lense–Thirring precession origin. *Mon. Not. R. Astron. Soc.* **2024**, *528*(2), 1668.
38. Ma, W. Q.; Gao, Z. F.; Li, B. P.; Niu, C. H.; Yao, J. M.; Wang, F. Y.. Reinvestigation of Fast Radio Burst Host Galaxy and Event Rate Density. *Astrophys. J.* **2025**, *981*(1), 24.
39. Wen, Z. G.; Yuan, J. P.; Wang, N.; Li, D.; Chen, J. L.; and Wang, P.; et al.. A Single-pulse Study of the Subpulse Drifter PSR J1631+1252 Discovered at FAST. *Astrophys. J.*, **2022**, **929** (1), 71.